Monthly Notices of the ROYAL ASTRONOMICAL SOCIETY

MNRAS **521,** 1988–2001 (2023) https://doi.org/10.1093/mnras/stad642
Advance Access publication 2023 March 2

Accurate analytic mass–scale relations for dark matter haloes of all masses and redshifts

Eduard Salvador-Solé,[1]★ Alberto Manrique,[1] David Canales[2] and Ignacio Botella[3]

[1]*Institut de Ciències del Cosmos i Departament de Física Quàntica i Astrofísica, Universitat de Barcelona. Martí i Franquès 1, E-08028 Barcelona, Spain*
[2]*Aerospace Engineering Department, Embry-Riddle Aeronautical University, 1 Aerospace Boulevard, Daytona Beach, Florida 32114, USA*
[3]*Department of Astronomy, Graduate School of Science, Kyoto University, Kitashirakawa, Oiwakecho, Sakyo-ku, Kyoto, 606-8502, Japan*

Accepted 2023 February 25. Received 2023 February 24; in original form 2022 November 11

ABSTRACT

CUSP is a powerful formalism that recovers, from first principles and with no free parameter, all the macroscopic properties of dark matter haloes found in cosmological *N*-body simulations and unveils the origin of their characteristic features. Since it is not restricted by the limitations of simulations, it covers the whole mass and redshift ranges. In the present Paper we use CUSP to calculate the mass–scale relations holding for halo density profiles fitted to the usual NFW and Einasto functions in the most relevant cosmologies and for the most usual mass definitions. We clarify the origin of these relations and provide accurate analytic expressions holding for all masses and redshifts. The performance of those expressions is compared to that of previous models and to the mass–concentration relation spanning more than 20 orders of magnitude in mass at $z = 0$ obtained in recent simulations of a 100 GeV WIMP universe.

Key words: methods: analytical – dark matter – cosmology: theory.

1 INTRODUCTION

Dark Matter (DM) haloes play a central role in cosmology. Unfortunately, owing to the difficulty of treating analytically DM clustering in the highly non-linear regime, their study has so far been carried out by means of *N*-body simulations with limited mass and force resolutions.

This is the reason that, besides a few studies on dwarf haloes with $M \sim 5 \times 10^8\, M_\odot$ at $z = 3 - 4$ (Moore et al. 2001; Colín et al. 2004; Ishiyama et al. 2013) and microhaloes with $M \sim 10^{-5}\, M_\odot$ and redshifts $z = 31 - 32$ (Anderhalden & Diemand 2013; Ishiyama 2014), halo density profiles have for a long time been determined for objects with masses $M \gtrsim 10^{10}\ M_\odot$ and redshifts $z \lesssim 2$ (see references below). Only very recently, simulations have managed to cover haloes with masses spanning 6 orders of magnitude (Ishiyama et al. 2020) and even 20 orders of magnitude (Wang et al. 2020) (hereafter WBFetal) at $z = 0$.

The usual way to deal with the halo density profiles drawn from simulations is by fitting them to the NFW (Navarro, Frenk & White 1995) or Einasto (Einasto 1965) parametric functions. Even though the fits are not perfect (Zhao et al. 2009; Muñoz-Cuartas et al. 2011) and introduce spurious effects (Salvador-Solé, Manrique & Solanes 2005), this procedure is sufficient for most purposes. One important result of that treatment is that the halo density profile appears to be universal except for the mass and redshift dependence of only one parameter (NFW 1996). A big effort has thus gone to determine those dependencies through the so-called mass-concentration, $M - c$, or characteristic mass-scale radius, $M_s - r_s$, relations dependent on z.

Simple analytic expressions, called 'toy models', were put forward that fit the relations found in simulations for haloes with $M \gtrsim 10^{10}\, M_\odot$ and $z \lesssim 3$ (e.g. Avila-Reese et al. 1999; Colín et al. 2004; Dolag et al. 2004; Gao et al. 2008; Duffy et al. 2008; Macciò et al. 2008; Zhao et al. 2009; Muñoz-Cuartas et al. 2011; Klypin, Trujillo-Gomez & Primack 2011; Prada et al. 2012; van den Bosch et al. 2014; Dutton & Macciò 2014; Sánchez-Conde & Prada 2014; Heitmann et al. 2015; Klypin et al. 2016; Child et al. 2018). These toy models show, however, significant differences between authors due to the different halo samples and data treatment employed. The largest divergence is found at the high-mass end due to the different virialization criteria used to get rid of haloes out of equilibrium (e.g. Ludlow et al. 2016 and references therein). Another more technical difference between those models is that some of them (Bhattacharya et al. 2013; Diemer, Kravtsov & More 2013a; Ludlow et al. 2014; Diemer & Kravtsov 2015; Diemer & Joyce 2019; see also Prada et al. 2012) treat the concentration c as a function of the halo seed height $\nu \equiv \delta/\sigma(M)$ instead of mass M.

With the aim to go beyond the M and z ranges covered by simulations some 'phenomenological' models were developed with a number of free parameters that were tuned through the fit to basically the same numerical data.

The phenomenological models of first generation relied on the empirical fact that halo concentration c decreases with increasing mass M (Navarro et al. 1996; Bullock, Kolatt & Siga Y. et 2001; Eke, Navarro & Steinmetz 2001; Neto et al. 2007; Macciò et al. 2008; Diemer & Kravtsov 2015). As in hierarchical cosmologies the smaller the mass of haloes, the earlier they form, that behaviour suggested that the central density of a halo should be proportional to the cosmic density at the halo formation time. Unfortunately, all these models led to an $M - c$ relation of the power-law form, while later simulations showed that the real $M - c$ relation flattens towards

★ E-mail: e.salvador@ub.edu

low-masses (Sánchez-Conde & Prada 2014; Ishiyama 2014; Ludlow et al. 2016).

The phenomenological models of second generation (Manrique et al. 2003; Salvador-Solé et al. 2007; Ludlow et al. 2014; Correa et al. 2015; Ludlow et al. 2016; Diemer & Joyce 2019) recovered that flattening. Manrique et al. (2003) took advantage of the fact that *accreting* haloes seem to grow inside-out (Salvador-Solé, Solanes & Manrique 1998; Huss, Jain & Steinmetz 1999) so that the mass accretion rate predicted e.g. in the extended-Press-Schecter (EPS) formalism (Press & Schechter 1974; Bond et al. 1991; Bower 1991; Lacey & Cole 1994) determined the halo density profile, with an $M - c$ relation that agreed with the results of simulations (Salvador-Solé et al. 2007). Correa et al. (2015) took the relation between the formation time and concentration found in simulations and also used the mass accretion history (MAH) of haloes predicted by the EPS formalism, while Ludlow et al. (2014) and Ludlow et al. (2016) followed the opposite scheme: they used the MAH found in simulations, which turns out to be very similar to their mass profile together with the halo formation time predicted by the EPS formalism (van den Bosch 2002). (Strictly speaking, the MAH of a halo refers to its 'mass *aggregation* history' rather than the mass *accretion* history because haloes grow not only through smooth accretion but also through major mergers.) Lastly, Diemer & Joyce (2019) relied on the observed constancy of the scale radius r_s of accreting haloes at the late accreting phase (Zhao et al. 2003; Lu et al. 2006; Salvador-Solé et al. 2005; Diemer, More & Kravtsov 2013b).

Interestingly, the inside-out growth of *accreting haloes* assumed by Manrique et al. (2003) is implicit in the three remaining models. Indeed, as assumed by Diemer & Joyce (2019), Correa et al. (2015) found that accreting haloes grow by keeping the scale radius unchanged as expected in inside-out growth, and the similarity between MAHs and mass profiles used by Ludlow et al. (2014) and Ludlow et al. (2016) is also implied by that growth. This suggests that the inside-out growth of accreting haloes supported by the results of simulations (e.g. Salvador-Solé et al. 1998; Fukushige & Makino 2001; Loeb & Peebles 2003; Zhao et al. 2003; Salvador-Solé et al. 2005; Lu et al. 2006; Romano-Díaz et al. 2006; Diemand, Kuhlen & Madau 2007; Cuesta et al. 2008; Wang et al. 2011; Ludlow et al. 2013) is crucial for the flattening of the $M - c$ relation. Yet, that evolution seemed too simplistic and was actually seen as a 'pseudo-evolution' (Diemer et al. 2013a; Wang et al. 2020a): haloes would apparently stretch outwards with increasing cosmic time even if they do not accrete simply because of the increase of the virial radius due to the decrease of the cosmic mean density. However, that argument is in contradiction with the fact that the density profile of haloes never falls off before the virial radius. Moreover, using the CUSP (*ConflUent System of Peak trajectories*) formalism (Manrique & Salvador-Solé 1995, 1996; Manrique et al. 1998), Salvador-Solé et al. (2012a) (see also Salvador-Solé & Manrique 2021) showed that the inside-out growth of accreting haloes is a natural consequence of the way accreted matter virializes.

As mentioned earlier, the Correa et al. (2015) model does not distinguish between smooth accretion and major mergers, but the other models do. In the Ludlow et al. (2016) and Diemer & Joyce (2019) models, the effects of major mergers were taken into account in specific non-trivial manners (see Section 5.2). Whereas Manrique et al. (2003) simply ignored them based on the assumption that violent relaxation causes haloes to loose the memory of their past history so that halo structure should not depend on their assembly process. That assumption seemed to contradict the 'assembly bias' found in simulations (Gottlöber, Klypin & Kravtsov 2001; Gottlöber et al. 2002; Sheth & Tormen 2004; Fakhouri & Ma 2009, 2010; Hahn et al. 2009; Chen et al. 2020; Ramakrishnan, Paranjape & Sheth 2021; Hellwing, Cautun & van de Weygaert 2021) suggesting that the halo density profile does depend on their merger history (e.g. Hester & Tasitsiomi 2010; Wang et al. 2020a). However, using CUSP, Salvador-Solé & Manrique (2021) have recently proven its validity, which explains the more compelling results of simulations showing that all halo properties (except for the subalo abundance, as also found by CUSP; see Salvador-Solé, Manrique & Botella 2022b) are independent of their assembly history (Wang & White 2009; Mao, Zentner & Wechsler 2018).

Thus, CUSP confirms the validity of the Manrique et al. (2003) model. But it does even better. It allows one to accurately derive *from first principles and with no single free parameter* all macroscopic properties of virialized haloes (in particular, their density profiles; Salvador-Solé et al. 2012a; Salvador-Solé et al. 2012b; Juan et al. 2014b) from the ellipsoidal collapse and virialization of their seeds, triaxial peaks (maxima) in the random Gaussian linear density field. It is thus much more powerful than any phenomenological model for the mass–scale relation.

In this Paper, we use it to infer very practical, accurate and physically motivated, analytic expressions for the mass–scale relations valid for all masses and redshifts in the most relevant cosmologies and usual halo mass definitions. In Section 2, we remind the derivation with CUSP of the mean spherically averaged halo density profile. Its fit to the usual NFW and Einasto analytic profiles is discussed in Section 3. The analytic expressions for the resulting $M - c$ and $M_s - r_s$ relations are given in Section 4 and their comparison to previous models relying on the results of simulations is carried out in Section 5. The results are summarized in Section 6.

2 THE DENSITY PROFILE PREDICTED BY CUSP

All macroscopic properties of haloes predicted by CUSP are in very good agreement with the results of simulations. The reader is referred to Salvador-Solé & Manrique (2021) for a comprehensive review of this formalism and the proofs of the two fundamental aspects of halo growth mentioned above. This is the case, in particular, of the spherically averaged density profile. Further, we briefly remind how it is derived (the corresponding numerical code is available from https://gitlab.com/cosmoub/cusp).

The ellipsoidal collapse time (along all three axes) of triaxial patches at some initial time t_i depends not only on their mass and size, but also on their shape and concentration (e.g. Peebles 1980). In other words, it is a function of the density contrast δ, smoothing radius R_f, ellipticity e, prolateness p, and curvature x of the corresponding peaks. However, the probability distributions functions of e, p and x of peaks with δ at R_f are very sharply peaked (Bardeen et al. 1986), so all patches traced by peaks with given δ and R_f have essentially the same values of e, p, and x and collapse at the same time. In other words, the ellipsoidal collapse time of patches essentially depends on δ and R_f of the peaks tracing them like in spherical collapse. Consequently, for any given $\delta(t)$ relation, we can find the radius R_f of the Gaussian filter such that the collapsing patches at t_i traced by peaks with δ at R give rise to haloes with mass M at t. Those $\delta(t)$ and $R_f(M, t)$ relations establish, by construction, a one-to-one correspondence between haloes with M at t and peaks with δ on R_f at t_i.

As shown by Juan et al. (2014a), these two relations, which depend on cosmology and halo mass definition, are fully determined by the consistency conditions that: (i) all the DM in the universe at any t is locked inside haloes and (ii) the mass M of haloes is equal to the

Table 1. Coefficients in the halo-peak correspondence.

Cosmology	Mass	d	s_0	s_1	s_2	A
WMAP7	$M_{\rm vir}$	1.06	0.0422	0.0375	0.0318	25.7
	M_{200}	1.06	0.0148	0.0630	0.0132	12.4
Planck14	$M_{\rm vir}$	0.928	0.0226	0.0610	0.0156	11.7
	M_{200}	0.928	0.0341	0.0684	0.0239	6.87

Table 2. Cosmological parameters.

Cosmology	Ω_Λ	$\Omega_{\rm m}$	h	$n_{\rm s}$	σ_8	Ω_b
WMAP7	0.73	0.27	0.70	0.97	0.81	0.046
Millennium	0.75	0.25	0.73	1.0	0.90	0.045
Planck14	0.68	0.32	0.67	0.96	0.83	0.049

volume-integral of their density profile. Specifically, if we write the density contrast δ for ellipsoidal collapse at t and the rms density fluctuation (or 0th-order spectral moment) $\sigma_0(R_{\rm f})$ of peaks in the density field at $t_{\rm i}$ filtered with a Gaussian window as proportional to the homologous quantities in top-hat spherical collapse (denoted by index th),

$$\delta(t,t_{\rm i}) = r_\delta(t)\,\delta^{\rm th}(t,t_{\rm i}) \tag{1}$$

$$\sigma_0(R_{\rm f},t,t_{\rm i}) = r_\sigma(M,t)\,\sigma_0^{\rm th}\left(R_{\rm f}^{\rm th},t_{\rm i}\right), \tag{2}$$

where $R_{\rm f}^{\rm th} = [3M/(4\pi)]^{1/3}$, $\delta^{\rm th}(t,t_{\rm i}) = \delta_{\rm c}^{\rm th}(t)D(t_{\rm i})/D(t)$, with $\delta_{\rm c}^{\rm th}(t)$ equal to the critical linearly extrapolated density contrast for spherical collapse at t and $D(t)$ equal to the linear growth factor, then the numerical functions r_δ and r_σ one is led to are well fitted, in all cases analysed, by the simple analytic expressions,

$$r_\delta(t) \approx \frac{a^d(t)}{D(t)} \tag{3}$$

and

$$r_\sigma(M,t) \approx 1 + S(t)r_\delta(t)\nu^{\rm th}(M,t)$$
$$S(t) = s_0 + s_1 a(t) + \log\left[\frac{a^{s_2}(t)}{1+a(t)/A}\right], \tag{4}$$

where $\nu^{\rm th}(M,t) \equiv \delta^{\rm th}(t,t_{\rm i})/\sigma_0^{\rm th}(R_{\rm f}^{\rm th},t_{\rm i}) = \delta_{\rm c}^{\rm th}(t)/\sigma_0^{\rm th}(M,t)$ is the (constant) linearly extrapolated top-hat height of the collapsing patch.

In Table 1, we provide the values of the coefficients in those fitting functions for the cosmologies (see Table 2) and mass definitions used in the simulations we will compare our predictions to. Those mass definitions, which arise from the use of the Spherical Overdensity (SO) halo-finding algorithm, correspond to haloes delimited by the radius R encompassing an overdensity $\Delta(z)$ relative to the characteristic cosmic density $\rho_\Delta(z)$: the 'virial mass', $M_{\rm vir}$, is for $\Delta(z)$ equal to the cosmology-dependent virial overdensity $\Delta_{\rm vir}(z)$ (e.g. Bryan & Norman 1998; Henry 2000) and $\rho_\Delta(z)$ equal to the mean cosmic density $\rho_{\rm cos}(z)$, whereas M_{200} is for a fixed value of $\Delta(z)$ equal to 200 and $\rho_\Delta(z)$ equal to the critical cosmic density $\rho_{\rm crit}(z)$.

Differentiating with respect to $R_{\rm f}$ the density field smoothed with a Gaussian filter, we obtain the differential equation

$$\frac{{\rm d}\delta}{{\rm d}R_{\rm f}} = -\langle x\rangle[\delta(R_{\rm f}),R_{\rm f}]\,\sigma_2(R_{\rm f})R_{\rm f}\,, \tag{5}$$

where $\langle x\rangle(\delta,R_{\rm f})$ is the mean curvature of peaks with δ at $R_{\rm f}$ and $\sigma_2(R_{\rm f})$ is the second order spectral moment. Given the one-to-one correspondence between haloes and peaks, ${\rm d}\delta/{\rm d}R_{\rm f}$ is related, through $\delta(t,t_{\rm i})$ and $M(R_{\rm f},t,t_{\rm i})$ given by equations (1) and (2), to the inverse of the instantaneous mass accretion rate of an accreting halo and the solution $\delta(R_{\rm f})$ is the continuous peak trajectory tracing its mass growth $M(t)$.

The trajectory $\delta(R_{\rm f})$ solution of equation (5) determines the *intrinsic* (i.e. unconvolved with respect to the smoothing window) mean spherically averaged density profile, $\rho_{\rm p}(r)$, of the protohalo. Indeed, taking the origin of the coordinate system at the peak on scale $R_{\rm f}$, the density contrast δ at ${\rm r_p} = 0$ is nothing but the convolution with the Gaussian window of that radius of the (i.e. unconvolved) density contrast field $\delta_{\rm p}({\rm r_p})$ in the protohalo. That is, after integrating over the polar angles, we have

$$\delta(R_{\rm f}) = \sqrt{\frac{2}{\pi}}\frac{1}{{R_{\rm f}}^3}\int_0^\infty {\rm d}r_{\rm p}\, r_{\rm p}^2\,\delta_{\rm p}(r_{\rm p})\exp\left(-\frac{r_{\rm p}^2}{2{R_{\rm f}}^2}\right), \tag{6}$$

where $\delta_{\rm p}(r_{\rm p})$ is the spherical average of $\delta_{\rm p}({\rm r_p})$. Consequently, given the *mean* peak trajectory $\delta(R_{\rm f})$ of purely accreting haloes with M at t, by solving the Fredholm integral equation of first kind in equation (6), we can find the mean density profile $\delta_{\rm p}(r_{\rm p})$ of their protohaloes (Salvador-Solé et al. 2012a).

Once we know the mean density profile $\delta_{\rm p}(r_{\rm p})$, we can calculate the mean total energy profile

$$E_{\rm p}(r_{\rm p}) = 4\pi\int_0^{r_{\rm p}} {\rm d}r\, r^2\rho_{\rm p}(r)\left\{\frac{\left[H_{\rm i}r - v_{\rm p}(r)\right]^2}{2} - \frac{GM_{\rm p}(r)}{r}\right\} \tag{7}$$

$$M_{\rm p}(r_{\rm p}) = 4\pi\int_0^{r_{\rm p}} {\rm d}r\, r^2\,\rho_{\rm p}(r), \tag{8}$$

where G is the gravitational constant, $\rho_{\rm p}(r_{\rm p})$ stands for $\rho_{\rm c}(t_{\rm i})[1+\delta_{\rm p}(r_{\rm p})]$, $H_{\rm i}$ is the Hubble constant at $t_{\rm i}$, and

$$v_{\rm p}(r_{\rm p}) = \frac{2G\left[M_{\rm p}(r_{\rm p}) - 4\pi r_{\rm p}^3\rho_{\rm c}(t_{\rm i})/3\right]}{3H(t_{\rm i})r_{\rm p}^2} \tag{9}$$

is the peculiar velocity caused by the mass excess within $r_{\rm p}$.

Monitoring the ellipsoidal collapse and virialization through shell crossing (though not apocentre crossing, which is at the base of the *inside-out growth* of the accreting haloes), we are led to the relation

$$r = -\frac{3}{10}\frac{GM^2}{E_{\rm p}(M)}\,. \tag{10}$$

between the radius r and mass M within it in the final virialized object (see Salvador-Solé et al. 2012a for details). Equation (10) resembles the virial relation for homogeneous systems with null confining pressure, but it differs from it in that $E_{\rm p}(M)$ is not the energy of the halo, $E(M)$, but that of the protohalo, which is not conserved during ellipsoidal collapse and shell crossing. Lastly, differentiating the profile $M(r)$ given by equation (10), we obtain the mean spherically averaged density profile $\rho(r)$ of virialized haloes with M at t.

We emphasize that, even though this profile has been derived assuming purely accreting haloes, it coincides with the profile of haloes of the same mass at the same cosmic time having suffered major mergers because, as shown in (Salvador-Solé & Manrique 2021), the violent relaxation suffered by haloes after a major merger causes them the memory loss of their past history. This fundamental result, formally proven in Salvador-Solé & Manrique (2021), is confirmed by the results of simulations (Ascasibar, Hoffman & Gottlöber 2007; Wang & White 2009; Mao et al. 2018).

3 ANALYTIC FITS TO THE DENSITY PROFILE

This theoretical mean spherically averaged halo density profile, which is numerical, can be fitted to the usual analytic expressions

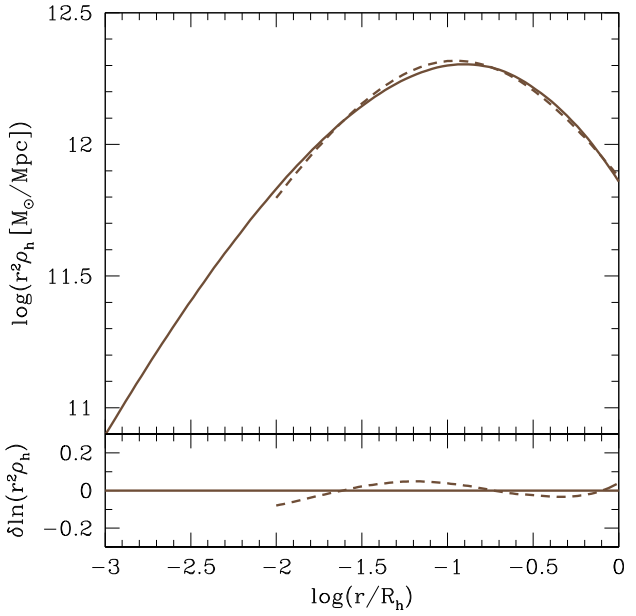

Figure 1. Mean spherically averaged density profile predicted by CUSP (solid line) for $z = 0$ haloes with $M_{\rm vir} = 10^{13}\,M_\odot$ in the *WMAP7* cosmology and its unconstrained best fit to the NFW function down to $10^{-2}R$ (dashed line).

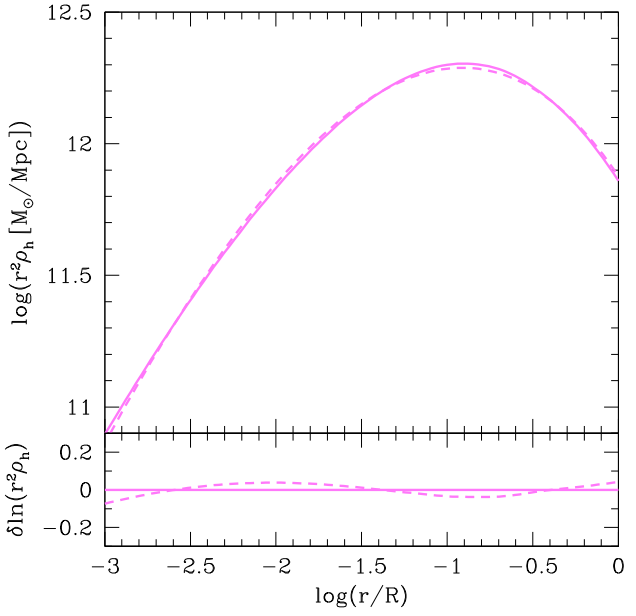

Figure 2. Same as Fig. 1 but for the Einasto fit down to $10^{-3}R$.

used for simulated haloes, namely the two-parametric NFW profile (Navarro et al. 1995),

$$\rho(r) = \rho_{\rm s}\frac{4r_{\rm s}^3}{r\,(r+r_{\rm s})^2}\,, \tag{11}$$

and the three-parametric Einasto profile (Einasto 1965),

$$\rho(r) = \rho_{\rm s}\exp\left\{-\frac{2}{\alpha}\left[\left(\frac{r}{r_{\rm s}}\right)^{\alpha}-1\right]\right\}\,, \tag{12}$$

where α is the so-called shape parameter. The parameters characterizing them are the scale radius $r_{\rm s}$ or the concentration $c \equiv R/r_{\rm s}$, where R is the radius of the halo, and the characteristic density $\rho_{\rm s}$ or the characteristic mass within $r_{\rm s}$,

$$M_{\rm s} = 16\pi\, f(1)\,\rho_{\rm s}\, r_{\rm s}^3, \tag{13}$$

with $f(x) = \ln(1+x) - x/(1+x)$, in the NFW case, or

$$M_{\rm s} = 2\pi\left(\frac{2}{\alpha}\right)^{1-\frac{3}{\alpha}} {\rm e}^{\frac{2}{\alpha}}\, f(1)\,\rho_{\rm s}\, r_{\rm s}^3\,, \tag{14}$$

with $f(x) = \Gamma(3/\alpha) - \Gamma(3/\alpha,\, 2x^{\alpha}/\alpha)$, where $\Gamma(x)$ and $\Gamma(x,\, y)$ are the gamma and incomplete gamma functions, respectively, in the Einasto case. Alternatively, one can use the total mass M, related to $M_{\rm s}$ through

$$M_{\rm s} = M\,\frac{f(1)}{f(c)}\,, \tag{15}$$

for the appropriate function $f(x)$ in the NFW and Einasto cases.

Note that parameters $r_{\rm s}$, $M_{\rm s}$ and α refer to the *internal* structure of haloes, which is kept fixed during inside-out growth, whereas parameters c and M involve their *global* structure, which varies as haloes grow. This is the reason why the relations between the former parameters are hereafter referred to as the 'internal relations' and the relations between the latter are referred to as 'global relations'.

Figs 1 and 2 illustrate the goodness of the analytic fits to the density profiles derived by means of CUSP. As can be seen, the fits are excellent, with the residuals having the typical S-shape found in simulations (e.g. Navarro et al. 2004). Moreover, not only do the theoretical density profiles have the same shape as the empirical ones but, as we will see in Section 5, the typical values of the fitting parameters also agree.

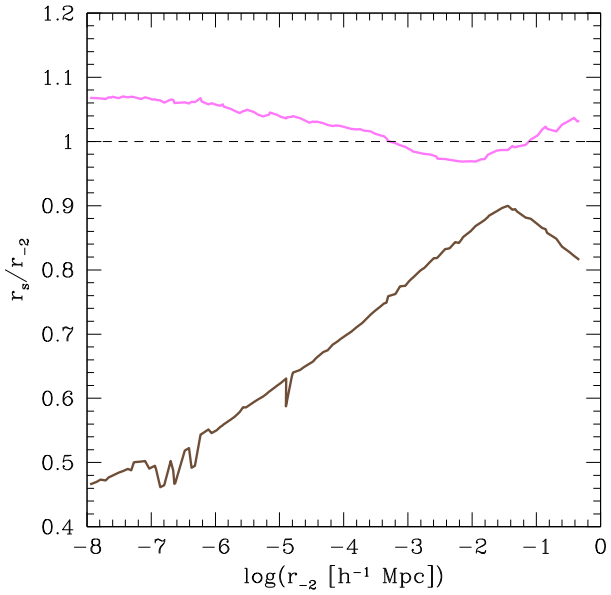

Figure 3. Best $r_{\rm s}$ values found in the non-parametric fits to the NFW (lower brown line) and the Einasto (upper pink line) of the density profiles predicted by CUSP for haloes with different r_{-2} values (corresponding to $M_{\rm vir}$ masses spanning from $10^{-5}\,M_\odot\,{\rm h}^{-1}$ to $10^{15}\,M_\odot\,{\rm h}^{-1}$) in the *WMAP7* cosmology at $z = 0$. (A colour version of this Figure is available in the online version of this Journal).

In Fig. 3, we compare the radius r_{-2}, where the logarithmic slope of the theoretical density profile is equal to -2, to the proxy $r_{\rm s}$ of the best fitting NFW and Einasto functions (equations [11] and [12]). While in the case of the Einasto profile the difference between r_{-2} and $r_{\rm s}$ is small ($1.06 \gtrsim r_{\rm s}/r_{-2} \gtrsim 0.96$) for haloes of all masses at $z =$

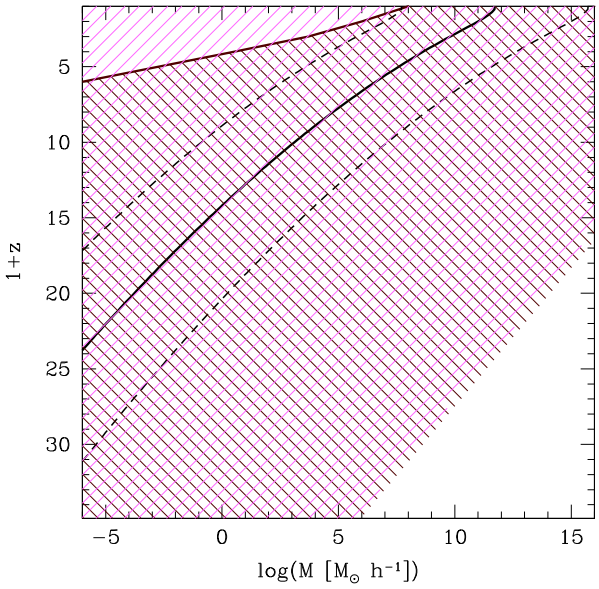

Figure 4. Domains of acceptability (according to the χ-square test) of the NFW (brown upper-left to lower-right hatched area) and Einasto (pink upper-right to lower-left hatched area) fits to the density profiles predicted by CUSP for haloes with M_{200} in the *WMAP7* cosmology with no free-streaming cutoff. The solid-black line marks the $M_*(z)$ curve and the dashed-black lines bracket the region $10^{-4} \leq M/M_*(z) \leq 10^4$ around it. (A colour version of this Figure is available in the online version of this Journal).

0 (a similar results is obtained at any other z), in the case of the NFW profile the solution is only acceptably good ($0.9 \gtrsim r_s/r_{-2} \gtrsim 0.8$) for large halo masses ($M \gtrsim 10^8\, M_\odot\, h^{-1}$). The reason for the better behaviour of the Einasto fitting function is, of course, that it involves more parameters. In the case of the NFW function r_s is smaller than r_{-2} (c larger than the real concentration), particularly at the low-mass end where the NFW function yields deficient fits to the very steep density profiles of low-mass haloes at low redshifts (see Fig. 4). In contrast, the Einasto fits are acceptable over the whole (M, z) plane.

By fitting the numerical profiles of haloes of all masses and redshifts, we have obtained the numerical dependence on M and z of the NFW and Einasto parameters, the so-called $M - c$ and $M_s - r_s$ relations, predicted by CUSP. Since those relations will be compared to those based on the results of simulations, we have fitted the numerical density profiles inferred by CUSP as done for the density profiles found in simulations: by χ^2 minimization over the radial range from R to $10^{-2}R$ with a constant logarithmic step. There are two possible ways to carry out the fits: keeping all the parameters free or enforcing their relation with the halo mass (or maximum circular velocity), which reduces the number of free parameters by one. In principle, letting all parameters free yields a better fit, but the mass of the halo with the best fitting density profile slightly differs from that of the real halo, so there is no clear advantage in any of the two procedures. In Section 5.2, where the CUSP-based $M - c$ relation will be compared to that found by WBFetal we will carry out unconstrained fits as done by those authors. However, in Section 5.1 where the models our predictions will be compared to use both kinds of fits, we will adopt the geometric mean of the values obtained in the two kinds of fits. This is enough, indeed, because the relative difference between the parameter values found in the two ways is small (<3 per cent at $10^{-4}\, M_*(z)$ and up to about 6 per cent at $M = 10^3\, M_*(z)$, where $M_*(z)$ is the critical mass for ellipsoidal collapse at z solution of the equation $\sigma[M_*(z), z] = \delta_c(z)$.

4 ANALYTIC MASS–SCALE RELATIONS

The fact that major mergers yield halo density profiles identical to those arising from accretion (Salvador-Solé & Manrique 2021), which develop inside-out, causes the typical spherically averaged density profiles of virialized haloes to be fully determined by those of peaks at t_i. The result is that halo density profiles are close to the NFW and Einasto form with the respective internal parameters satisfying very simple relations.

Indeed, the $M_{-2} - r_{-2}$ relation, with $M_{-2} \equiv M(r_{-2})$, is basically a power law. The reason for this is that both $\sigma_2(R_f)$ and $\langle x \rangle[\delta(R_f), R_f]$ are closely power laws (in the halo mass range, the CDM power spectrum behaves as a power law) and so is also the mean trajectory $\delta(R_f)$ of accreting haloes (equation [5]). Since the boundary condition δ at $R_f(M, t)$ is also close to a power law of M (equation [2]), the whole solution $\delta(R_f)$ will essentially behave as a power law of M at every fixed R_f too. And the same is true for the *unconvolved* protohalo density contrast $\delta_p(r)$ at any fixed r, which implies that the total energy of protohaloes $E_p(M)$ is also closely a power law of M (equations [29] – [30] in Salvador-Solé et al. 2012a). Equation (10) then implies that the mass M inside the radius r along the evolution of any accreting halo is approximately a power law too, with the same index for all haloes, which explains that the $M_{-2} - r_{-2}$ relation in all accreting haloes approximately satisfies the same linear log–log relation.

Therefore, since r_s is a good proxy for r_{-2} (Fig. 3), the $M_s - r_s$ relation must be close to a power law,

$$r_s = r_0 \left(\frac{M_s}{M_0}\right)^\tau , \tag{16}$$

with index τ independent of mass. Moreover, as r_s and M_s are internal parameters, τ must also be independent of z. And, as can be seen by dividing equation (13) by equation (14), the third internal parameter, α, must also have an approximately fixed value at least for large masses where both the NFW and Einasto profiles provide acceptable fits.

Strictly speaking, since the power-law form of r_s (equation [16]) is just a good approximation, τ and α will slightly depend on M_s. Moreover, since the fit of the density profiles to the usual analytic functions is not perfect, the best fitting values of the internal parameters will also slightly vary with z due to the variation of the fitted radial range with halo growth (Salvador-Solé et al. 2012a). Consequently, we must allow for τ and α to slightly depend on both M_s and z.

The expressions

$$\frac{\tau}{\tau_0} = 1 + t_1(1+z)^{t_2}\left[\frac{M_s}{M_0(1+z)^{t_3}}\right]^{t_4} \tag{17}$$

and

$$\frac{\alpha}{\alpha_0} = 1 + \alpha_1(z)\left\{1 + \left[\frac{M_c(z)}{M_s}\right]^{\frac{1}{2}}\right\}^{\alpha_2(z)} + \left\{1 + \left[\frac{M_s}{M_c(z)}\right]^{\frac{1}{2}}\right\}^{\alpha_3} , \tag{18}$$

with

$$\alpha_1(z) = a_{1,1}\,[1 - a_{1,2}\,\mathrm{erf}(z)]$$
$$\alpha_2(z) = a_{2,1}(1 - z/2)^{a_{2,2}}$$
$$\log[M_c(z)] = \log(M_1)\exp(m\,z)\,,$$

Table 3. Coefficients in the NFW and Einasto $M_s - r_s$ relations.

Cosmology	Mass	Profile	r_0 (10^{-5} Mpc)	M_0 ($M_\odot$)	τ_0	t_1	t_2	t_3	t_4
WMAP7	M_{vir}	NFW	9.46	1.00×10^5	0.325	0.183	− 0.192	− 0.346	.0145
		Einasto	10.2	8.91×10^4	0.311	0.213	− .0234	0	.0183
	M_{200}	NFW	9.75	1.00×10^5	0.317	0.199	− 0.124	− 0.221	.0134
		Einasto	10.8	8.91×10^4	0.325	0.155	− .0325	0	.0224
Planck14	M_{vir}	NFW	8.04	1.00×10^5	0.280	0.382	− 0.113	− 0.349	.00854
		Einasto	8.91	8.91×10^4	0.344	.0717	− 0.117	0	.0467
	M_{200}	NFW	8.59	1.00×10^5	0.314	0.219	− 0.134	− 0.238	.0134
		Einasto	10.0	8.91×10^4	0.353	.0510	− 0.100	0	.0503
Planck14*	M_{200}	Einasto	10.1	8.91×10^4	0.347	.0673	–	–	.0388

Note. *Mass-unconstrained fit with α fixed according to equation (18) with coefficients given in Table 4.

Table 4. Coefficients in the Einasto $M_s - \alpha$ relation.

Cosmology	Mass	M_1 ($M_\odot$)	m	α_0	$a_{1,1}$	$a_{1,2}$	$a_{2,1}$	$a_{2,2}$	α_3
WMAP7	M_{vir}	2.63×10^{10}	− 0.0648	0.317	− 1.275	0.0348	0.00434	0.445	− 0.0523
	M_{200}	0.69×10^{10}	− 0.0615	0.290	− 1.189	0.0306	0.00449	0.545	− 0.0538
Planck14	M_{vir}	7.66×10^{10}	− 0.0543	0.300	− 1.250	0.0457	0.00487	0.621	− 0.0502
	M_{200}	1.89×10^{10}	− 0.0355	0.300	− 1.219	0.0287	0.00478	0.455	− 0.0605
Planck14*	M_{200}	9.43×10^9	− 0.0542	0.302	− 1.204	–	0.00396	–	–

Note. *Mass-unconstrained three-parametric fit.

where erf is the error function, give excellent fits to the numerical relations predicted by CUSP. In Tables 3 and 4 we provide the best values of the coefficients for the cases of interest used in this work.

Taking into account the definition of concentration, $c = R/r_s$, and equation (15), the previous internal relations lead to the $M - c$ relation

$$\log(c) + \tau(M,z)\log\left[\frac{f(1)}{f(c)}\right] = \frac{1}{3}\log\left[\frac{[M/M_0]^{1-3\tau(M,z)}}{\mu(z)}\right] \quad (19)$$

$$\mu(z) = \frac{4\pi\,\Delta(z)\rho_\Delta(z)\,r_0^3}{3M_0} \quad (20)$$

with $\tau(M,z)$ given by equation (17) and the $M - \alpha$ relation given by equation (18) with M_s replaced by $Mf(1)/f(c)$. Note that the $M - \alpha$ relation has an extra implicit dependence on z through c.

The goodness of the previous analytic fitting expressions for the NFW and Einasto $M_s - r_s$ and $M - c$ relations is seen in Figs 5, 6, and 7, where they are compared to the numerical relations directly arising from the fits to the halo density profiles predicted by CUSP for different cosmologies and mass definitions (see Section 5). The large oscillations found in the best fitting values of α (Fig. 7) show the difficulty of determining this parameter due to the degeneracy in the three-parametric fit. Fortunately, the best values of the other two parameters, r_s and ρ_s (or M_s) are weakly dependent on the exact value of α, so they are well determined anyway (see Fig. 6).

We remark that, while the $M_s - r_s$ and $M_s - \alpha$ relations (equations [16] – [18]) are explicit for r_s and α, the $M - c$ and $M - \alpha$ relations are implicit for c and α, so the former are more practical than the latter. Nevertheless, in small mass ranges the dependence of c on M can be approximated by a simple power-law relation as found in classical toy models. Indeed, $f(c)$ is essentially constant[1] and τ is little dependent on M, so the $M - c$ relation in equation (19) is close to a linear log–log relation. On the other hand, the same approximations (i.e. $f(c)$ constant and $\tau \approx 1/3$) also lead to

$$c \propto [\Delta(z)\rho_\Delta(z)]^{-1/3}\,, \quad (21)$$

[1] $f(c)$ is a smooth function of c, and c is little dependent on M because τ is close to 1/3.

implying that c is roughly proportional to $(1+z)^{-1}$ in small redshift ranges as found by Bullock et al. (2001), though equation (21) is a better approximation.

5 COMPARISON WITH PREVIOUS MODELS

The comparison of those CUSP-based analytic mass–scale relations to previous toy and phenomenological models will be achieved in the two different mass and redshift regimes probed by simulations and for both the 'global' and 'internal' relations. These two kinds of relations are equivalent, but, while the former is the most commonly used, the latter informs more directly on halo growth.

There are of course small differences in the data treatment and fitting procedure used by different authors (including ourselves), but they are not expected to significantly affect the comparisons. The only differences that, in principle, might substantially affect them are: (i) while the concentration obtained by means of CUSP refers to the *mean* density profile of haloes with a given mass, that considered in most models is the *median* value and (ii) while CUSP deals by definition with virialized haloes, simulations include to some extent haloes out of equilibrium. Point (i) could be a problem because the concentration of haloes of a given mass is lognormally distributed with a notable scatter (Dutton & Macciò 2014), implying that the mean concentration is substantially larger than the median one. However, the concentration calculated by means of CUSP is not the mean concentration of haloes with fixed mass, but the concentration of the mean density profile of those haloes and, as shown in the Appendix, this latter value coincides with the median concentration. Thus, there is no problem in this respect. Regarding point (ii), we must say that the departure from equilibrium of haloes really causes the $M - c$ and $M_s - r_s$ relations at the high-mass end at every redshift to differ between different models and the CUSP-based ones. Indeed, a large fraction of simulated haloes in that mass regime, where major mergers are more common, are not fully relaxed and, even though the authors enforce different virialization criteria in order to select

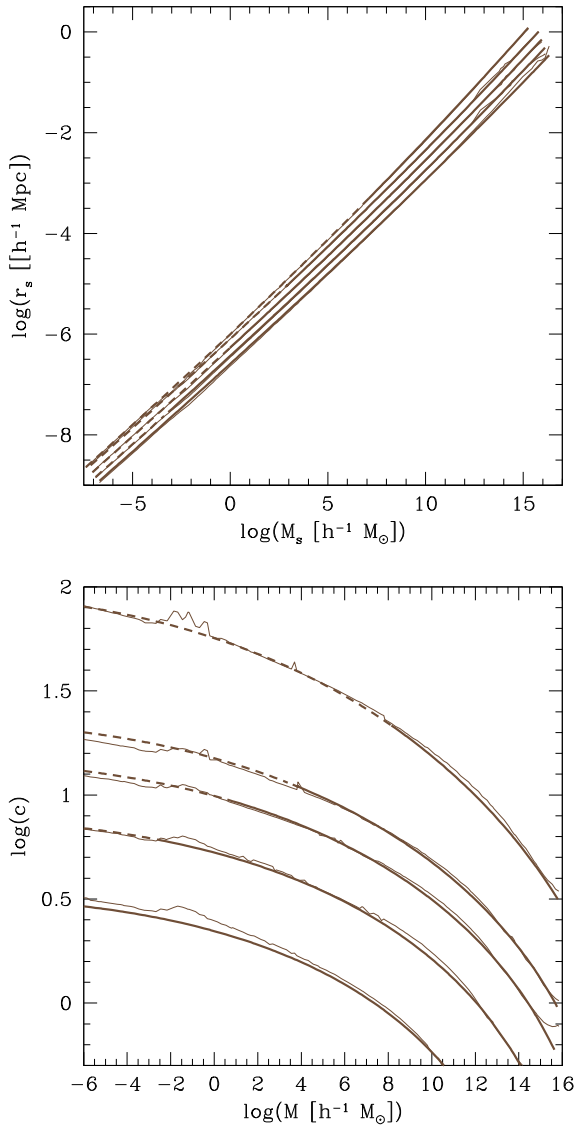

Figure 5. Top panel: $M_s - r_s$ relations resulting from the fits to the NFW profile of the halo density profiles predicted by CUSP in the *WMAP7* cosmology (thin lines) and the corresponding fits to the analytic equation (16)-(17) (thick lines) for all relevant M_{vir} masses and $z = 0$, 2, 3, 5, and 9 (from top to bottom). To avoid overlapping the curves for $z > 0$ have been progressively shifted 0.2 dex downwards. The regions where the NFW fits are deficient are marked with dashed lines. Bottom panel: same as the top panel, but for the $M - c$ relations using the analytic equation (19). No shift has been applied to these curves.

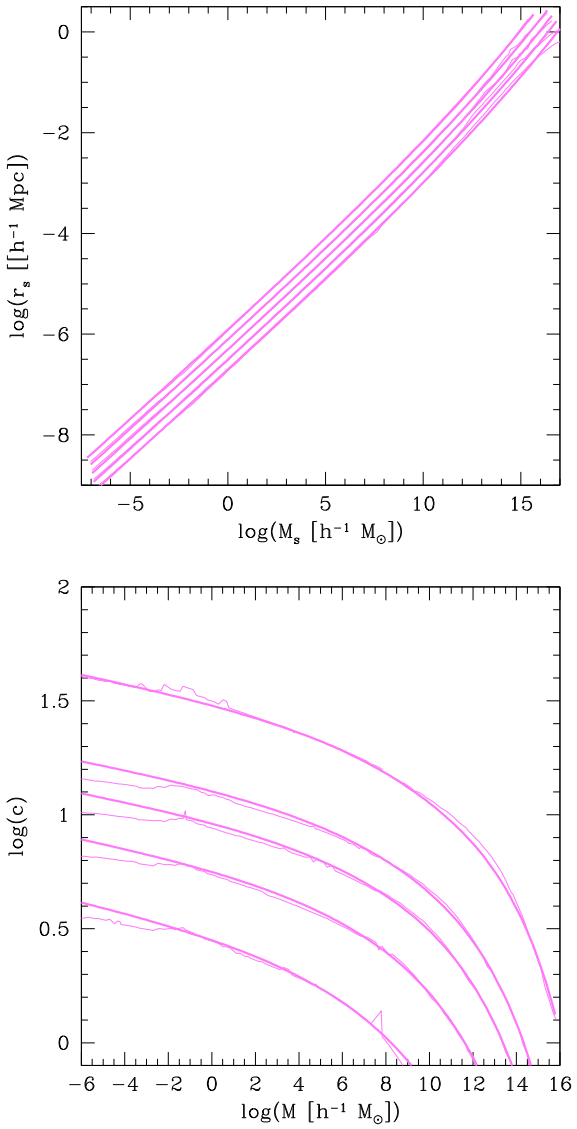

Figure 6. Same as Fig. 5 but for the Einasto profile and M_{200} masses in the *Planck14* cosmology (thin and thick lines). Top panel: $M_s - r_s$ relations. Bottom panel: corresponding $M - c$ relations.

those which are, this objective is not fully accomplished (Ludlow et al. 2016).

5.1 High-mass low-redshift regime

Further, we compare our analytic relations to previous toy models in the high-M low-z regime.

Among all the models focusing on the NFW profile we have chosen those provided by Zhao et al. (2009), Muñoz-Cuartas et al. (2011) and Klypin et al. (2011) since they all refer to the same *WMAP7* cosmology (Komatsu et al. 2011) or close to it (see Table 2) and the same M_{vir} masses, which we also adopt for the CUSP-based relations. Other more recent toy models (Prada et al. 2012; Dutton & Macciò 2014; Klypin et al. 2016; Ishiyama et al. 2020) using other cosmologies, parametrizations or fitting techniques give similar results, however. We must also say that Zhao et al. (2009) and Muñoz-Cuartas et al. (2011) adjust two parameters, while Klypin et al. (2011) adjust only one parameter (they enforce the value of the maximum circular velocity V_{max}). This is the reason why we use the hybrid fit technique explained in Section 3.

For the Einasto profile, the toy models available are those provided by Gao et al. (2008) for the *Millennium* cosmology (with parameters close to the Planck ones; see the parameters values in Table 2) (Springle et al. 2005) and by Dutton & Macciò (2014) and Klypin et al. (2016) for the *Planck14* cosmology (Planck Collaboration et al. 2014; Klypin et al. 2016) (see Table 2). The masses adopted in all those studies are M_{200}. We thus use the CUSP-based relations for that cosmology and mass definition. Again, Gao et al. (2008) and Dutton & Macciò (2014) used unconstrained fits, while Klypin et al. (2016) used constrained ones. Ludlow et al. (2013) repeated the study by Gao et al. (2008) for the same cosmology and with more

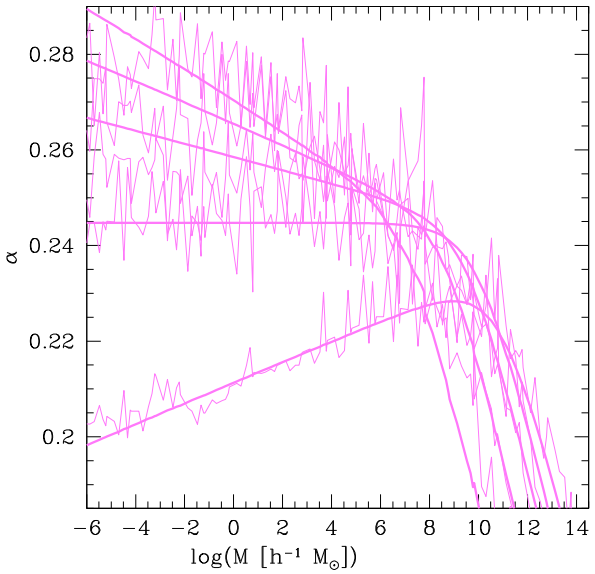

Figure 7. Same as Fig. 6 for the $M - \alpha$ relations. The lowest curve on the left corresponds to $z = 0$, and the uppermost one to $z = 9$.

particles per halo, but they focus on $z = 0$, so we compare our analytic expressions to the former model.

As the fit to the three-parametric Einasto function is somewhat degenerate, the simulations employed to build the latter models use many more particles per halo than in the NFW case so as to better determine the halo density profiles. But then halo samples have substantially higher mass limits, which makes it difficult to determine reliable $M - \alpha$ relations. To alleviate this problem, Gao et al. (2008) replace this relation between α and M by another one between α and the time-invariant linear (top-hat) height $\nu^{\rm th}(M, z) \equiv \delta_{\rm c}^{\rm th}(z)/\sigma^{\rm th}(M, z)$ of protohaloes with M at z, which compresses the scatter in the data. Of course, this procedure does not break the degeneracy in α; it just smooths out the relation. The price to pay for this is that any real trend in the data is harder to detect. Dutton & Macciò (2014) adopted the same relation found by Gao et al. (2008) and Klypin et al. (2016) just repeated the fit. Thus, the fact that the $M - \alpha$ curves derived from the $\nu^{\rm th} - \alpha$ relations inferred from all three authors essentially coincide does not make them more reliable. On the contrary, they are the relations worst determined. Fortunately, the uncertainty in α has little effect on the associated $M - c$ relation (e.g. Gao et al. 2008; see also Section 5.2).

In all Figures below, the curves predicted by CUSP, from now on called 'theoretical relations', are plotted in thick solid line even though there should be essentially no halo in equilibrium with masses $M > 10^3 M_*(z)$, where the typical time elapsed since the last major merger is smaller than a few $(2 - 3)$ crossing times (Raig, González-Casado & Salvador-Solé 2001). Regarding the curves of the toy models, from now on called 'empirical relations', they are plotted in thin solid line within the mass range covered by the data, and in thin-dashed line their extrapolations beyond that mass range.

5.1.1 *Global relations*

The theoretical and empirical NFW $M - c$ relations are compared in Fig. 8, top panel. At $z = 0$ all the curves are quite similar. In particular, the theoretical relation fully coincides with the toy model by Zhao et al. (2009). However, they markedly differ at the high-mass end. While the theoretical curve keeps on decreasing at

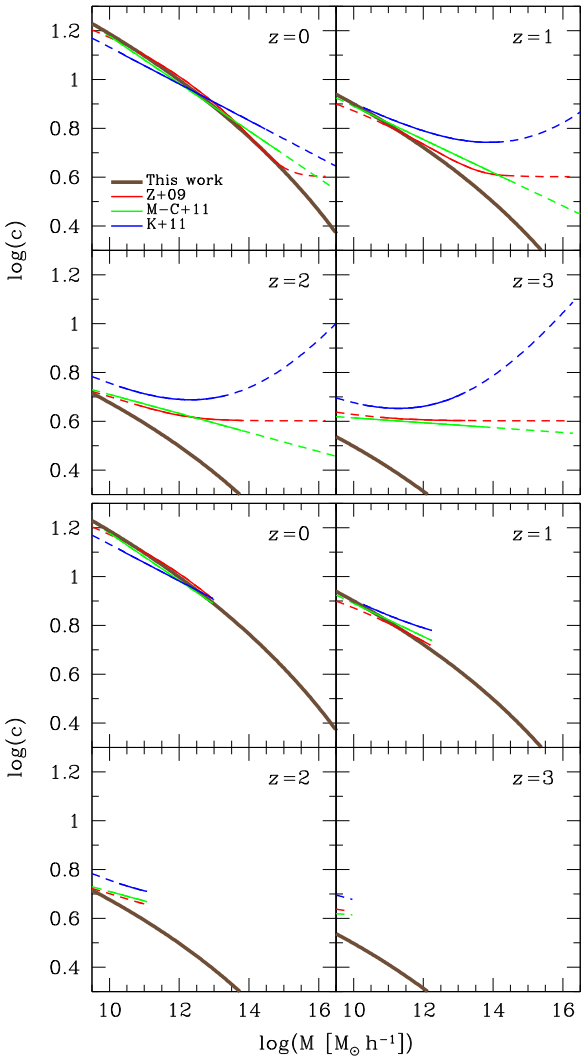

Figure 8. Top panels: comparison between the NFW $M - c$ relation predicted by CUSP and provided by the toy models by Zhao et al. (2009), Muñoz-Cuartas et al. (2011) and Klypin et al. (2011) at different redshifts for $M_{\rm vir}$ masses in essentially the same *WMAP7* cosmology. Bottom panels: same as top panels, but for the toy models restricted to masses $M < 10\,M_*(z)$. (A colour version of this Figure is available in the online version of this Journal).

the same accelerated rate, the empirical curves change their trends unexpectedly: the curve corresponding to the toy model by Zhao et al. (2009) suddenly levels off and those of the toy models by Muñoz-Cuartas et al. (2011) and Klypin et al. (2011) keep on decreasing at a constant rate and bend upwards, respectively. The same divergent behaviour of the toy models is observed at higher redshifts, though at progressively smaller masses. Only when the curves are truncated at $10\,M_*(z)$ are they much similar to each other (see Fig. 8, bottom panel) and to our predictions.

In the Einasto case (see Fig. 9), the result is similar except for the fact that there is a more marked discrepancy between the theoretical predictions and the toy models as well as between the toy models themselves. This is likely due to the fact that, for the above mentioned reasons, the empirical curves are restricted to more massive haloes than in the NFW case, which are the most affected by the departure from equilibrium. Only the toy model by Klypin et al. (2016) reaches moderately massive haloes and the corresponding $M - c$ curves are indeed the closest to the theoretical ones. But the largest discrepancy

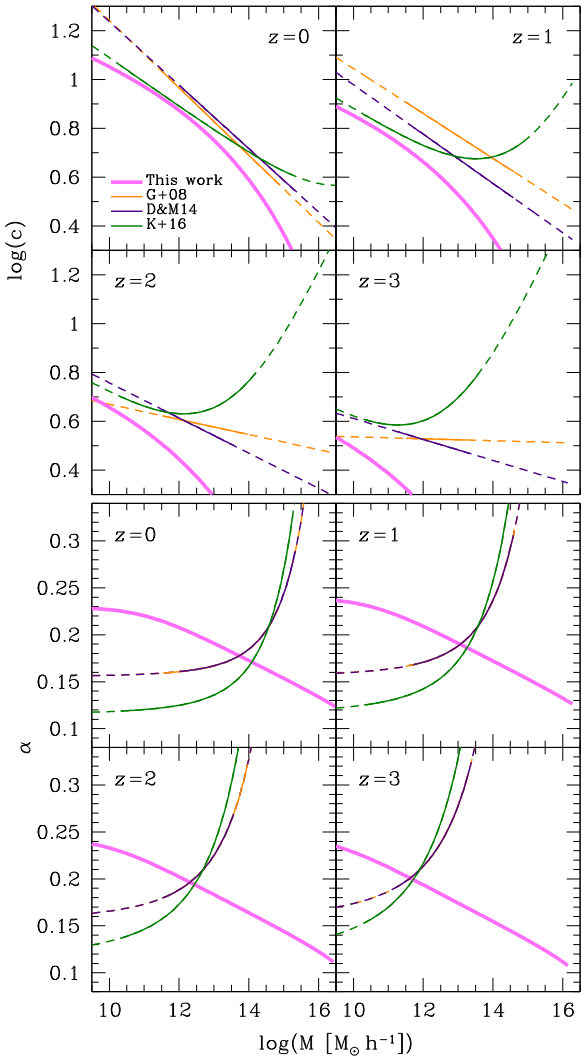

Figure 9. Top panels: same as the top panels of Fig. 8 for the Einasto $M - c$ relation predicted by CUSP and the toy models by Gao et al. (2008), Dutton & Macciò (2014) and Klypin et al. (2016) at different redshifts for M_{200} masses in several *Plank14*-like cosmologies. Bottom panels: same as top panels for the $M - \alpha$ relations. (A colour version of this Figure is available in the online version of this Journal).

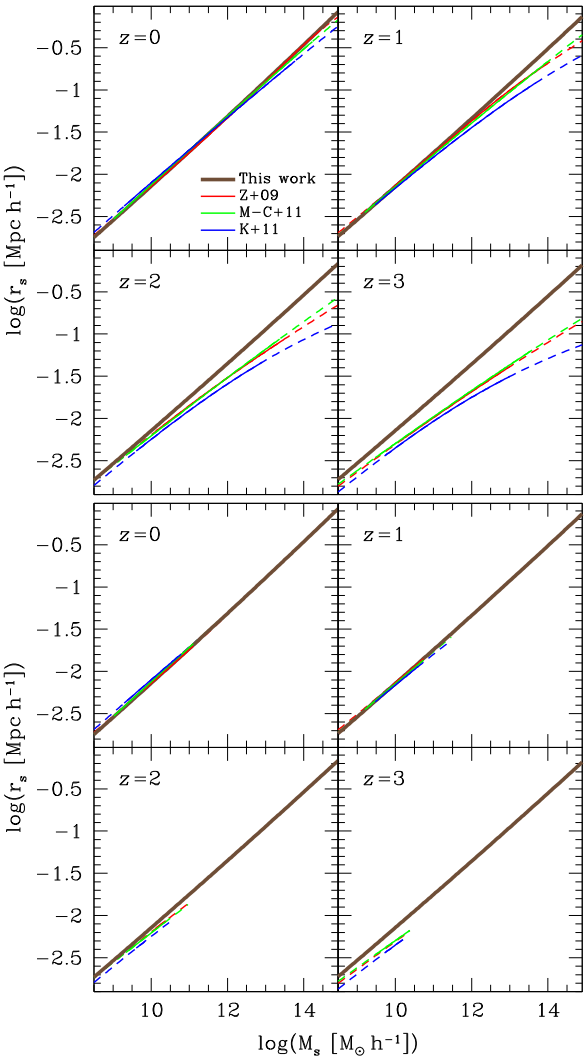

Figure 10. Top panels: same as Fig. 8, but for the NFW $M_s - r_s$ relations. Bottom panels: same as top panels, but restricted to haloes with masses $M < 10\,M_*(z)$. (A colour version of this Figure is available in the online version of this Journal).

is in the $M - \alpha$ relations. While α is little dependent on M and z in the theoretical curves, it markedly depends on both arguments in the empirical ones. We recall that there is a large degeneracy in the α parameter so that the $M - \alpha$ relation is quite uncertain. The fact that the empirical $M - \alpha$ curves are very similar to each other does not mean they are more reliable than the theoretical ones. They are similar simply because Dutton & Macciò (2014) adopted the same $M - \alpha$ relation as Gao et al. (2008) and Klypin et al. (2016) fitted their own data with identical $\nu^{\rm th} - \alpha$ functionality. Interestingly, at $z = 0$ the theoretical $M - \alpha$ curve is consistent, between $10^{11}\,M_\odot\,{\rm h}^{-1}$ and $10^{15}\,M_\odot\,{\rm h}^{-1}$, with a constant value of α of about 0.18 as found by Ludlow et al. (2016) in their simulations restricted to that mass range and redshift.

To sum up, for haloes with masses $M < 10\,M_*(z)$ at $z \lesssim 2$ there is good agreement between the theoretical global relations and previous toy models targeting masses $M > 10^{10}\,h^{-1}\,{\rm M}_\odot$. These results indicate that $10\,M_*(z)$ mark the upper mass limit at each redshift for halo samples not to be affected by the departure from equilibrium of those objects. The comparison regarding the $M - \alpha$ relation in the Einasto case is little compelling due to the big uncertainty affecting this relation in the toy models considered and the marked departure from equilibrium of very massive haloes as included in the toy models dealing with the Einasto profile. Klypin et al. (2011) found, indeed, that the fit of the density profiles of haloes out of equilibrium leads to higher values of α than in relaxed haloes, where it is close to $\alpha \approx 0.18$ (see also Klypin et al. 2016), which agrees with the results by Ludlow et al. (2016) at $z = 0$ and with our predictions.

5.1.2 *Internal relations*

In Fig. 10, top panel, we see that, at $z = 0$, all NFW $M_s - r_s$ curves essentially overlap in the same approximate power-law relation. As z increases, the logarithmic slope of the empirical curves slightly shifts at the high-mass end where it varies notably from author to author. This suggests that the different behaviour of the theoretical an empirical curves at high-masses at every z simply reflects the above mentioned bias introduced by haloes out

of equilibrium. Indeed, when the curves are truncated at $10\,M_*(z)$ (Fig. 10, bottom panel), not only do they all essentially coincide with each other but also with the thoeretical curves. On the contrary, the slope of the theoretical relation remains much more constant with varying redshift, as expected. In fact, the only slight change disappears when the fit is carried over the same radial range at all redshifts.

The Einasto relations are shown in Fig. 11. The theoretical $M_s - r_s$ and $M_s - \alpha$ curves for different z now almost coincide even without taking a fixed fitting radial range (see top and middle panels). This reflects the fact that the Einasto function provides better fits to the halo density profiles than the NFW function due to the extra parameter α (see Fig. 3). On the contrary, the empirical curves show a marked dependence on z, even more marked than for the NFW profile (Fig. 10), likely due to the slight coupling of r_s with the poorly determined α parameter, whose wrong dependence on z artificially boosts that of r_s. Once again, when the relations are truncated at $10\,M_*(z)$, all the $M_s - r_s$ curves almost fully overlap and their dependence on z disappears (we have skipped this figure to avoid being repetitive). However, the corresponding empirical $M_s - \alpha$ curves, depicted in Fig. 11 bottom panel, still get apart from the theoretical one and show a marked dependence on z.

The conclusion of the comparison of the internal relations is that, in the mass range $M \lesssim 10 M_*(z)$, where most haloes are in equilibrium, the toy models behave as predicted by CUSP: the $M_s - r_s$ relation is close to a time-invariant power law, and the dependence of α on M_s is much less marked and closer to constant than found at large masses, according to the predictions of CUSP. Since it is very unlikely that these results are simultaneously met for other causes, they give strong support to the halo growth conditions evidenced by CUSP. Unfortunately, the mass range (of two orders of magnitude) and the redshift interval (below $z = 2$ only) covered by those toy models are too narrow to be more conclusive in this respect.

5.2 Whole mass range at redshift zero

This limitation is amply overcome by the simulation recently performed by WBFetal at $z = 0$ in a flat Lambda 100 Gev WIMP universe with the *Plank14* cosmological parameters (see Table 2). These authors fitted the empirical $M - c$ relation found for M_{200} masses to the Einasto relation (with unconstrained fits). We can thus check the validity of the Einasto CUSP-based analytic expressions derived for those cosmology and mass definition over the whole mass range.

WBFetal studied two cases: with and without free-streaming mass cut-off of the CDM power spectrum. For simplicity, we concentrate here on the case of no cut-off, though CUSP can also deal with a mass cut-off (see Viñas, Salvador-Solé & Manrique 2012). To this end we have carried out unconstrained fits to the density profiles predicted by CUSP in the same cosmology and for the same mass definition and derived the analytic $M - c$ and $M - \alpha$ relations (see the resulting values of the coefficients in Tables 3 and 4).

In Figure 12, we depict the M_{200}–α relation obtained from those fits. Like in Fig. 7, the best values of α show large oscillations, though its trend is quite well determined anyway, particularly in the range $-3 \lesssim \log(M_{200}/\mathrm{M}_\odot) \lesssim 7$. Nevertheless, the values of the other two parameters, M_s (or ρ_s) and r_s, are very well determined. This is important because, even though our α values deviate from

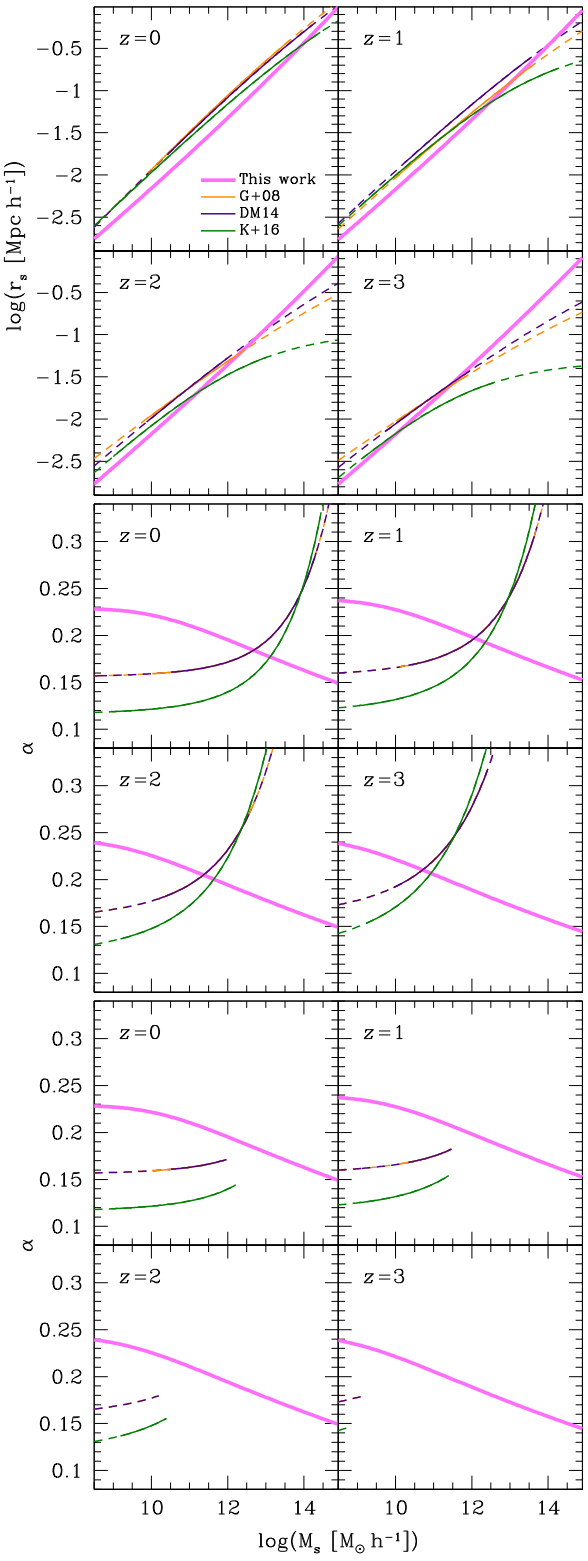

Figure 11. Top panels: same as Fig. 9, but for the $M_s - r_s$ relations. Middle panels: corresponding $M_s - \alpha$ relations. Bottom panels: same as middle panels, but restricted to haloes with $M < 10\,M_*(z)$. (A colour version of this figure is available in the online version of this Journal.).

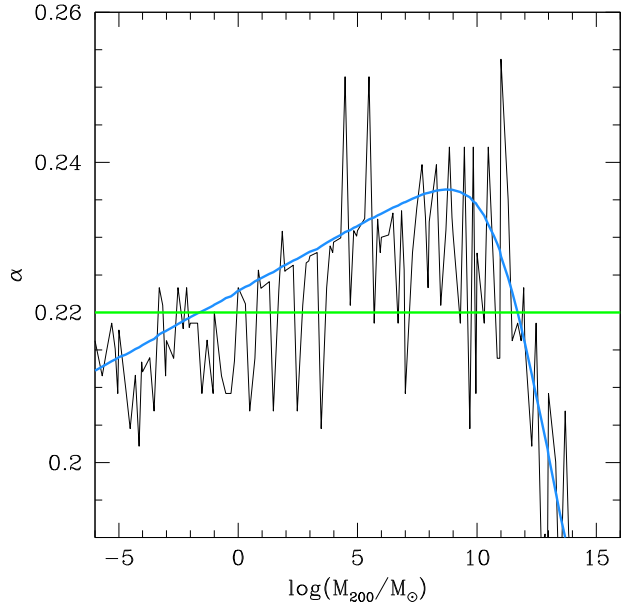

Figure 12. Raw M_{200}–α relation (black line) resulting from unconstrained fits to the Einasto function of the density profiles of current haloes predicted by CUSP (with no free-streaming mass cut-off) over the whole mass range analysed by WBFetal in the same cosmology. We also plot the best $\alpha(M_{200})$ fit according to the analytic expression (18) with $M_s = Mf(1)/f(c)$ (blue line) and a constant α value of 0.22 (green line). To avoid overlapping with the raw relation, the blue curve has been shifted upwards by 0.001. (A colour version of this Figure is available in the online version of this Journal).

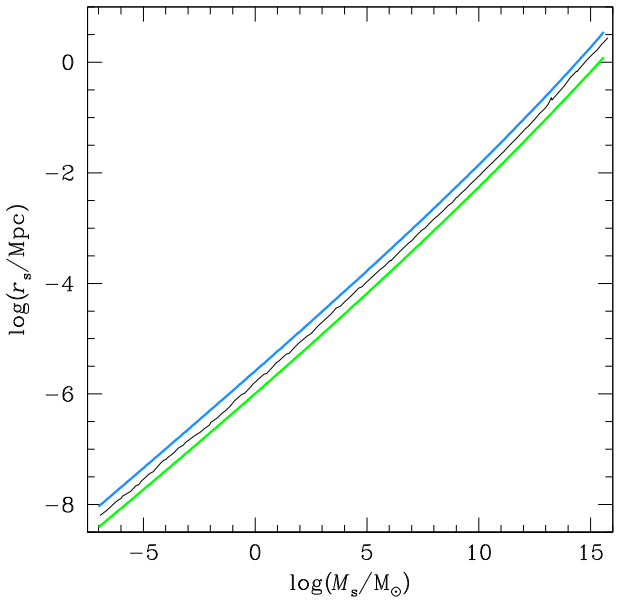

Figure 13. Same as Fig. 12, but for the r_s and M_s values resulting from the unconstrained (triparametric) fits to the density profiles predicted by CUSP (black line) and from the constrained (biparametric) fits using the two $\alpha(M_{200})$ relations plotted in Fig. 12: the one according to the equation (18) (blue line) and the other one with $\alpha = 0.22$ (green line). To avoid overlapping these two latter curves have been shifted 0.2 dex upwards and downwards, respectively. (A colour version of this Figure is available in the online of this Journal).

those around 0.16 found by WBFetal,[2] the corresponding $M_s - r_s$ relation is very stable and insensitive to the exact α values. Indeed, as shown in Figure 13, the raw r_s and M_s values arising from the unconstrained fits with oscillating α values are essentially identical to those found by fixing α according to the analytic equation (18) or taking it fixed and equal to 0.22. Indeed, a constant α as adopted by WBFetal is also a good approximation since the absolute variation in the value of this parameter over 15 orders of magnitude (between the maximum at $\log(M_{200}) \sim 9$ and the low-mass end at $\log(M_{200}) \sim -6$) is only of $\sim$0.02. As can be seen, the two theoretical $M_s - r_s$ relations obtained in that way are almost identical and close to a straight line over more than 20 orders of magnitude, as expected.

The corresponding $M - c$ relations are depicted in Fig. 14 where they are compared to the empirical $M - c$ relation found by WBFetal from the fits to the density profiles of simulated haloes (with fixed α equal to 0.16). As can be seen, there is good agreement between both $M - c$ relations: the largest difference between the two curves over more than 20 orders of magnitude at $M_{200} \sim 10^9\,M_\odot$ is just a factor $\sim$1.15 and much smaller than the rms scatter of the empirical c values. That agreement is particularly remarkable given that the WBFetal $M - c$ relation was obtained by linking by hand the relations obtained in a mosaic of 8 narrow mass ranges which do not exactly match each other and even substantially deviate from the general trend adopted (see their Fig. 3), meaning that this empirical relation could locally somewhat deviate from the real relation.

[2]The reason for that difference could be due to the fact that WBFetal fit the staked density profiles in a different range of radii above an unspecified (possibly mass-dependent) 'convergence radius' larger than $10^{-3}R_{200}$.

In Fig. 14, we also depict the $M - c$ relations obtained from several phenomenological and toy models. Among all those $M - c$ relations, the ones showing a global trend similar to that of the WBFetal relation are the phenomenological models by Correa et al. (2015), Ludlow et al. (2014) (in its latest version given in Ludlow et al. 2016) and, at a lesser extent, by Diemer & Joyce (2019). As mentioned earlier, all these models rely on (or are consistent with) the fact that haloes grow inside-out during accretion as found in CUSP. But what about their treatment of major mergers? Do they also implicity assume that the density profile arising from major mergers is indistinguishable from that of haloes grown by smooth accretion?

The equality between the mass profile and MAH of haloes at the base of Ludlow et al. (2014) model rigorously holds for purely accreting haloes only. When a halo undergoes a major merger its mass suddenly increases by a factor of about two, while the mean (or critical) cosmic density does not change. Major mergers thus cause discontinuities in the halo MAHs that are not reflected in their mass profiles which are necessarily continuous. There should thus be a small trend for halo MAHs to decline slightly more steeply than their mass profiles at high-z, where major mergers are more frequent (e.g. Zhao et al. 2003). That trend is indeed observed in the comparison between the two kinds of profiles made in Ludlow et al. (2014) (see their Fig. 4). Fortunately, this effect is expected to only affect the density profile derived from the MAH at very small radii, typically smaller than r_s, so it should not affect the $M - c$ relation derived in this way. Only for haloes with very low masses near the free-streaming cut-off where essentially the whole density profile is set during the initial rapid growth phase (with very frequent major mergers) should this effect have noticeable consequences for the $M - c$ relation derived from MAHs. But Ludlow et al. 2016 changed their model in that mass regime. Instead of monitoring MAHs, they monitor the history of the collapsed mass, that is, all the mass that is eventually assembled in the final object regardless of

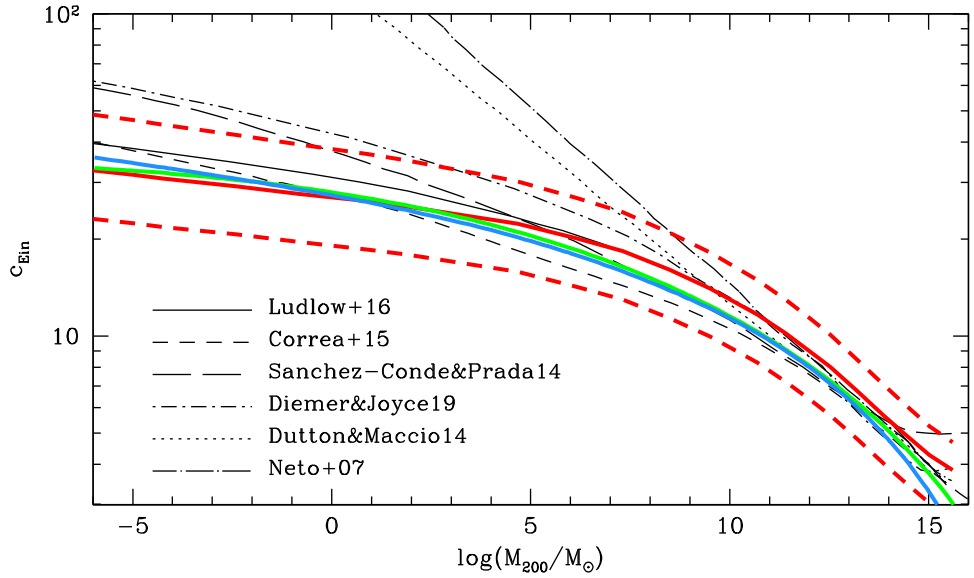

Figure 14. Same as Fig. 13 (same lines and colours), but for the M_{200}–c relation (the blue and green lines are not shifted now and almost overlap). For comparison we plot the M_{200}–c relation (for median c values) found by WBFetal by fitting the density profiles of simulated haloes to the Einasto profile with a fixed value of α of 0.16 (solid red line) and the corresponding typical rms scatters (dashed red lines). The $M - c$ relations predicted by other phenomenological and toy models are also shown (black lines). (A colour version of this Figure is available in the online version of this Journal).

whether it comes from the main progenitor. When doing this, these authors implicitly follow what would be the putative MAH of the final halo had it been evolving by *pure accretion* thanks to the fact that, as considered in CUSP, the density (and mass) profile of haloes emerging from major mergers is indistinguishable from that of purely accreting haloes. It is thus unsurprising that the model by Ludłow et al. 2016 shows a similar good behaviour than the CUSP-based model. The Ludłow et al. 2016 model is just slightly less accurate because it uses the EPS formalism instead of CUSP. We remark also that it includes two free parameters, while the CUSP-based model is parameter-free.

In the models by Correa et al. (2015) and Diemer & Joyce (2019), the inside-out growth implied by the constancy of the scale radius is only seen at the late phase of their evolution. In Correa et al. (2015) model this is not important because the model does not rely on whether accreting haloes grow inside-out or not, it just relies on the mass aggregation history predicted by the EPS model without making the distinction between smooth accretion and major mergers. However, the Diemer & Joyce (2019) model explicitly assumes that, during the late accretion (or pseudo-accretion) phase haloes grow inside-out by keeping the $r_{\rm s}$ unchanged. In the initial phase dominated by major mergers, it is assumed that it is the concentration c which is kept approximately constant. This approximation not only complicates the model (it harbours five free parameters because of the necessity to define the frontier between the two different growth phases dependent on halo mass), but it is not accurate enough. If c were really kept constant in major mergers, $M_{\rm s}$ would be kept essentially proportional to M_{200} (equation [15]) and, since R_{200} is proportional to M_{200} to the 1/3, $r_{\rm s}$ should also be proportional to $M_{\rm s}$ to the 1/3. It is true that, according to the predictions of CUSP, τ is not far from 1/3 (see the value of τ_0 in Tab. 3), which explains that the Diemer & Joyce (2019) model yields acceptable predictions. However, it slightly deviates from this value depending on mass (and redshift), which causes the $M - c$ relation predicted by the Diemer & Joyce (2019) model not to flatten enough.

The conclusion of the comparison over the full halo mass range is thus that the predictions of CUSP agree with the results of numerical simulations over the full mass range of 20 orders of magnitude at $z = 0$. The fact that the phenomenological models of second generation that recover the flattening of the $M - c$ relation include implicitly the inside-out growth of accreting haloes and implicitly the similarity of the density profiles of haloes regardless of their assembly history gives strong support to such growth conditions explicitly accounted for in CUSP (and proven in Salvador-Solé & Manrique 2021).

6 SUMMARY AND CONCLUSIONS

The CUSP formalism allows one to accurately derive from first principles and with no free parameter all macroscopic halo properties (including substructure; Salvador-Solé, Manrique & Botella 2022a; Salvador-Solé et al. 2022b; Salvador-Solé et al. 2022) and to clarify the origin of all their features (Salvador-Solé & Manrique 2021). In this Paper, it has been applied to derive the mass–scale relations satisfied by halo density profiles. Specifically, we have analysed how the two fundamental characteristics of halo growth evidenced by CUSP, namely that accreting haloes grow inside-out and that haloes having suffered major mergers are indistinguishable from those having grown by pure accretion, translate into those relations.

We have shown that such characteristics lead to an intrinsic $M_{-2} - r_{-2}$ relation of the real non-parametric density profiles that is time-invariant and very close to a power law with index τ around 1/3. However, the proxy relation $M_{\rm s} - r_{\rm s}$ and the global shape parameter α found from the fit of the profiles to the usual NFW and Einasto parametric functions slightly deviate from those simple trends due to the fact that these functionalities do not yield a perfect fit, so, even though accreting haloes grow inside-out, the best fitting values of the internal and shape parameters, $r_{\rm s}$, $M_{\rm s}$, and α, slightly shift with mass and redshift as the total fitted radial range expands.

We have shown that, while the Einasto function gives acceptable fits to the halo density profile over the whole mass and redshift range, the NFW function is only acceptable, at low-z, for high-masses.

Simple analytic expressions have been provided that give very good fits to the 'internal' $M_s - r_s$ and $M_s - \alpha$ relations, as well as to the 'global' $M - c$ and $M - \alpha$ relations for haloes of all masses and redshifts obtained from the fitting to the NFW and Einasto functions of the non-parametric halo density profiles predicted by CUSP. Even though the two kinds of relations are equivalent, the former are more practical given their simpler form. In particular, the $M - c$ relation is far from a power law as found in some classical toy models; it progressively flattens in log-log towards low-masses. On the other hand, it shows a dependence on redshift which differs from a simple power law of $1 + z$ as also found in some phenomenological models.

The performance of our CUSP-based analytic $M - c$ and $M_s - r_s$ relations and the associated $M - \alpha$ and $M_s - \alpha$ relations in the Einasto case has been compared to that of several toy models holding at high masses ($M \gtrsim 10^{10} h^{-1}\,\mathrm{M}_\odot$) and low redshifts ($z \lesssim 2$), as well as to several phenomenological models supposed to cover all halo masses. We find good agreement between the predicted $M - c$ and $M_s - r_s$ relations and the toy models provided halo masses stay below $10\,M_*(z)$ at any redshift. At higher masses the agreement deteriorates due to the fact that the predictions of CUSP are for virialized haloes, whereas simulated haloes with higher masses progressively get apart from equilibrium (an increasing fraction of them have suffered a too recent major merger and have had no time to relax). Regarding the $M - \alpha$ and $M_s - \alpha$ relations, our predictions substantially deviate from those found by Gao et al. (2008) at very high masses where haloes are out of equilibrium. They are, however, consistent with a roughly constant value of $\alpha \sim 0.18$ as found by Ludlow et al. (2016).

On the other hand, we have found good agreement with the empirical Einasto $M - c$ relation recently derived by WBFetal from a simulation of haloes at $z = 0$ with masses spanning more than 20 orders of magnitude. The relations predicted by CUSP behave slightly better than any other phenomenological model put forward so far including those of Correa et al. (2015), Ludlow et al. (2016) and Diemer & Joyce (2019). We have shown that the latter models, which also behave reasonably well, also implicitly assume the earlier mentioned fundamental characteristics of halo growth accounted for by CUSP and proven in Salvador-Solé & Manrique (2021). These characteristics were also assumed in the old phenomenological model by Manrique et al. (2003) using of the EPS formalism. However, the new mass–scale relations derived here from the CUSP formalism are more accurate and practical and arise from first principles, that is, they do not rely on any arguable assumption and do not use any free parameter.

ACKNOWLEDGEMENTS

This work was funded by grants CEX2019-000918-M (Unidad de Excelencia 'María de Maeztu') and PID2019-109361GB-100 (together with FEDER funds) by MCIN/AEI/10.13039/501100011033, and by the grant number 2017SGR643 by the Catalan DEC.

7 DATA AVAILABILITY

The data underlying this article will be shared on reasonable request to the corresponding author.

REFERENCES

Anderhalden D., Diemand J., 2013, JCAP, 2013, 009
Ascasibar Y., Hoffman Y., Gottlöber S., 2007, MNRAS, 376, 393
Avila-Reese V., Firmani C., Klypin A., Kravtsov A. V., 1999, MNRAS, 310, 527
Bardeen J. M., Bond J. R., Kaiser N., Szalay A. S., 1986, ApJ, 304, L15
Bhattacharya S., Habib S., Heitmann K., Vikhlinin A., 2013, ApJ, 766, L32
Bond J. R., Cole S., Efstathiou G., Kaiser N., 1991, ApJ, 379, L440
Bower R. G., 1991, MNRAS, 248, 332
Bryan G. L., Norman M. L., 1998, ApJ, 495, L80
Bullock J. S., Kolatt T. S., Siga Y., Sommerville R. S., Kravtsov A. V., Klypin A. A., Primack J. R., Dekel A., 2001, MNRAS, 321, 559
Chen Y., Mo H. J., Li C., Wang H., Yang X., Zhang Y., Wang K., 2020, ApJ, 899, L81
Child H. L., Habib S., Heitmann K., Frontiere N., Finkel H., Pope A., Morozov V., 2018, ApJ, 859, L55
Colín P., Klypin A., Valenzuela O., Gottlöber S., 2004, ApJ, 612, L50
Correa C. A., Wyithe J. S. B., Schaye J., Duffy A. R., 2015, MNRAS, 452, 1217
Cuesta A. J., Prada F., Klypin A., Moles M., 2008, MNRAS, 389, 385
Diemand J., Kuhlen M., Madau P., 2007, ApJ, 667, L859
Diemer B., Joyce M., 2019, ApJ, 871, L168
Diemer B., Kravtsov A. V., 2015, ApJ, 799, L108
Diemer B., Kravtsov A. V., More S., 2013, ApJ, 779, L159
Diemer B., More S., Kravtsov A. V., 2013, ApJ, 766, L25
Dolag K., Bartelmann M., Perrotta F., Baccigalupi C., Moscardini L., Meneghetti M., Tormen G., 2004, A&A, 416, 853
Duffy A. R., Schaye J., Kay S. T., Dalla Vecchia C., 2008, MNRAS, 390, 64
Dutton A. A., Macciò A. V., 2014, MNRAS, 441, 3359
Einasto J., 1965, Trudy Inst. Astrofiz. Alma-Ata, 5, 87
Eke V. R., Navarro J. F., Steinmetz M., 2001, ApJ, 554, L114
Fakhouri O., Ma C.-P., 2009, MNRAS, 394, 1825
Fakhouri O., Ma C.-P., 2010, MNRAS, 401, 2245
Fukushige T., Makino J., 2001, ApJ, 557, L533
Gao L., Navarro J. F., Cole S., Frenk C. S., White S. D. M., Springel V., Jnekins A., Neto A. F., 2008, MNRAS, 387, 536
Gottlöber S., Klypin A., Kravtsov A. V., 2001, ApJ, 546, L223
Gottlöber S., Kerscher M., Kravtsov A. V., Faltenbacher A., Klypin A., Müller V., 2002, A&A, 387, 778
Hahn O., Porciani C., Dekel A., Carollo C. M., 2009, MNRAS, 398, 1742
Heitmann K. et al., 2015, ApJS, 219, 34
Hellwing W. A., Cautun M., van de Weygaert R., Jones B. T., 2021, Phys. Rev. D, 103, 063517
Henry J. P., 2000, ApJ, 534, L565
Hester J. A., Tasitsiomi A., 2010, ApJ, 715, L342
Huss A., Jain B., Steinmetz M., 1999, ApJ, 517, L64
Ishiyama T., 2014, ApJ, 788, L27
Ishiyama T., Rieder S., Makino J., Portegies Zwart S., Groen D., Nitadori K., de Laat C., et al., 2013, ApJ, 767, L146
Ishiyama T. et al., 2020, preprint (arXiv:2007.14720)
Juan E., Salvador-Solé E., Domènec G., Manrique A., 2014a, MNRAS, 439, 719
Juan E., Salvador-Solé E., Domènech G., Manrique A., 2014b, MNRAS, 439, 3156
Klypin A. A., Trujillo-Gomez S., Primack J., 2011, ApJ, 740, L102
Klypin A., Yepes G., Gottlöber S., Prada F., Heß S., 2016, MNRAS, 457, 4340
Komatsu E., et al., 2011, ApJS, 192, 18
Lacey C., Cole S., 1994, MNRAS, 271, 671
Loeb A., Peebles P. J. E., 2003, ApJ, 589, L29
Lu Y., Mo H. J., Katz N., Weinberg M. D., 2006, MNRAS, 368, 1931
Ludlow A. D. et al., 2013, MNRAS, 432, 1103
Ludlow A. D. et al., 2014, MNRAS, 441, 378
Ludlow A. D., Bose S., Angulo R. E., Wang L., Hellwing W. A., Navarro J. F., Cole S., Frenk C. S., 2016, MNRAS, 460, 1214
Macciò A. V., Dutton A. A., van den Bosch F. C., 2008, MNRAS, 391, 1940
Manrique A., Salvador-Solé E., 1995, ApJ, 453, L6
Manrique A., Salvador-Solé E., 1996, ApJ, 467, L504
Manrique A., Raig A., Solanes J. M., González-Casado G., Stein P., Salvador-Solé E., 1998, ApJ, 499, 548

Manrique A., Raig A., Salvador-Solé E., Sanchis T., Solanes J. M., 2003, ApJ, 593, L26
Mao Y.-Y., Zentner A. R., Wechsler R. H., 2018, MNRAS, 474, 5143
Moore B., Calcáneo-Roldán C., Stadel J., Quinn T., Lake G., Ghigna S., Governato F., 2001, Phys. Rev. D, 64, 063508
Muñoz-Cuartas J. C., Macciò A. V., Gottlöber S., Dutton A. A., 2011, MNRAS, 411, 584
Navarro J. F., Frenk C. S, White S. D. M., 1995, ApJ, 275, L720
Navarro J. F., Frenk C. S., White S. D. M., 1996, ApJ, 462, L563
Navarro J. F., et al., 2004, MNRAS, 349, 1039
Neto A. F. et al., 2007, MNRAS, 3381, 1450
Peebles P. J. E., 1980, Large-Scale Structure of the Universe by Phillip James Edwin Peebles. Princeton Univ. Press, p. 1980 ISBN: 978-0-691-08240-0
Planck Collaboration et al., 2014, A&A, 571, 16
Prada F., Klypin A. A., Cuesta A. J., Betancort-Rijo J. E., Primack J., 2012, MNRAS, 423, 3018
Press W. H., Schechter P., 1974, ApJ, 187, L425
Raig A., González-Casado G., Salvador-Solé E., 2001, MNRAS, 327, 939
Ramakrishnan S., Paranjape A., Sheth R. K., 2021, MNRAS, 503, 2053
Romano-Díaz E., Faltenbacher A., Jones D., Heller C., Hoffman Y., Shlosman I., 2006, ApJ, 637, L93
Salvador-Solé E., Manrique A., 2021, ApJ, 914, L141
Salvador-Solé E., Solanes J. M., Manrique A., 1998, ApJ, 499, L542
Salvador-Solé E., Manrique A., Solanes J. M., 2005, MNRAS, 358, 901
Salvador-Solé E., Manrique A., González-Casado G., Hansen S. H., 2007, ApJ, 666, L181
Salvador-Solé E., Viñas J., Manrique A., Serra S., 2012, MNRAS, 423, 2190
Salvador-Solé E., Serra S., Manrique A., González-Casado G., 2012b, MNRAS, 424, 3129
Salvador-Solé E., Manrique A., Canales D., Botella I., 2022, MNRAS, 511, 641
Salvador-Solé E., Manrique A., Botella I., 2022, MNRAS, 509, 5305
Salvador-Solé E., Manrique A., Botella I., 2022, MNRAS, 509, 5316
Sánchez-Conde M. A., Prada F., 2014, MNRAS, 442, 2271
Sheth R. K., Tormen G., 2004, MNRAS, 350, 1385
Springel V. et al., 2005, Nature, 435, 629
van den Bosch F. C., 2002, MNRAS, 331, 98
van den Bosch F. C., Jiang F., Hearin A., Campbell D., Watson D., Padmanabhan N., 2014, MNRAS, 445, 1713
Viñas J., Salvador-Solé E., Manrique A., 2012, MNRAS, 424, 6
Wang J., White S. D. M., 2009, MNRAS, 396, 709
Wang J. et al., 2011, MNRAS, 413, 1373
Wang K., Mao Y.-Y., Zentner A. R., Lange J. U., van den Bosch F. C., Wechsler R. H., 2020, MNRAS, 498, 4450
Wang J., Bose S., Frenk C. S., Gao L., Jenkins A., Springel V., White S. D. M., 2020, Nature, 585, 39
Zhao D. H., Mo H. J., Jing Y. P., Börner G., 2003, MNRAS, 339, 12
Zhao D. H., Jing Y. P., Mo H. J., Börner G., 2009, ApJ, 707, L354

APPENDIX A: MEDIAN CONCENTRATION AND MEAN-PROFILE CONCENTRATION

The mean density profile of haloes of a given virial or M_{200} mass M and the corresponding radius R is, like the density profile of individual haloes of that mass, approximately of the NFW or Einasto form. Thus, according to equations (13) or (14) and equation (15), the characteristic density of the mean density profile, $\rho_s(\langle\rho\rangle)$, equal to the mean density of individual haloes at the scale radius $r_s(\langle\rho\rangle)$, satisfies the relation

$$M = f[R/r_s(\langle\rho\rangle)]C\rho_s(\langle\rho\rangle)r_s^3(\langle\rho\rangle), \tag{A1}$$

where C is a constant equal to 16π and $2\pi(2/\alpha)^{1-\frac{3}{\alpha}}\exp(2/\alpha)$ in the cases of the NFW and Einasto profiles, respectively, and $f(x)$ is the corresponding function. On the other hand, the characteristic density ρ_s at the scale radius r_s of each individual halo satisfies the same relation

$$M = f[R/r_s]C\rho_s r_s^3. \tag{A2}$$

We thus have

$$\Delta\ln r_s = \frac{1}{3}\left(\ln\left\{\frac{f[R/r_s(\langle\rho\rangle)]}{(R/r_s)}\right\} - \Delta\ln\rho_s\right), \tag{A3}$$

with $\Delta\ln r_s = \ln r_s - \ln[r_s(\langle\rho\rangle)]$ and $\Delta\ln\rho_s = \ln\rho_s - \ln\rho_s(\langle\rho\rangle)$. Taking into account the relation

$$\ln\rho_s = \ln\rho_s(\langle\rho\rangle) + \left.\frac{\mathrm{d}\ln\rho}{\mathrm{d}\ln r}\right|_{\ln r_s}\Delta\ln r_s, \tag{A4}$$

valid to first order, where, by definition of scale radius, the logarithmic derivative in the right-hand member is equal to -2, we arrive at

$$\Delta\ln r_s = \ln\left\{\frac{f[R/r_s(\langle\rho\rangle)]}{f(R/r_s)}\right\} + \frac{\Delta\rho_s}{\rho_s(\langle\rho\rangle)}, \tag{A5}$$

where $\Delta\rho_s = \rho[r_s(\langle\rho\rangle)] - \rho_s(\langle\rho\rangle)$. Note that $\rho[r_s(\langle\rho\rangle)]$ is the density of each individual halo at the scale radius of the mean density profile.

Taking into account that $f(x)$ is a very smooth function of x, the term $\ln\{f[R/r_s(\langle\rho\rangle)]/f(R/r_s)\}$ in equation (A5) can be neglected. Thus, dividing r_s and $r_s(\langle\rho\rangle)$ by R, equation (A5) can be rewritten in the form

$$\frac{c}{c(\langle\rho\rangle)} \approx \exp\left[\frac{\Delta\rho_s}{\rho_s(\langle\rho\rangle)}\right]. \tag{A6}$$

Since $c/c(\langle\rho\rangle)$ is lognormally distributed (Dutton & Macciò 2014), equation (A6) implies that $\Delta\rho_s/\rho_s(\langle\rho\rangle)$ is (approximately) normally distributed. Moreover, since the mean of the latter variable is null, we conclude that the median of $c/c(\langle\rho\rangle)$ is $\exp(0) = 1$ or, equivalently, that the median concentration of haloes with M very nearly coincides with the concentration of the mean density profile, $c(\langle\rho\rangle)$.

This paper has been typeset from a TEX/LATEX file prepared by the author.